Shear small-angle light scattering studies of shear-induced concentration fluctuations and steady state viscoelastic properties

Endoh, Maya K.; Takenaka, Mikihito; Inoue, Tadashi; Watanabe, Hiroshi; Hashimoto, Takeji

THE JOURNAL OF CHEMICAL PHYSICS **128**, 164911 (2008)

Shear small-angle light scattering studies of shear-induced concentration fluctuations and steady state viscoelastic properties

Maya K. Endoh,[1] Mikihito Takenaka,[1] Tadashi Inoue,[2] Hiroshi Watanabe,[3] and Takeji Hashimoto[1,4,a)]

[1]*Department of Polymer Chemistry, Graduate School of Engineering, Kyoto University, Kyoto 615-8510, Japan*
[2]*Department of Macromolecular Science, Faculty of Science, Osaka University, Osaka 560-0042, Japan*
[3]*Institute for Chemical Research, Kyoto University Uji, Kyoto 611-0011, Japan*
[4]*Japan Atomic Energy Agency, Advanced Science Research Center, Tokai-mura, Ibaraki 319-1195, Japan*

(Received 14 December 2007; accepted 27 February 2008; published online 30 April 2008)

We aimed at elucidating the influence of shear-induced structures (shear-enhanced concentration fluctuations and/or shear-induced phase separation), as observed by rheo-optical methods with small-angle light scattering under shear flow (shear-SALS) and shear-microscopy, on viscoelastic properties in semidilute polystyrene (PS) solutions of 6.0 wt % concentration using dioctyl phthalate (DOP) as a Θ solvent and tricresyl phosphate (TCP) as a good solvent. In order to quantify the effects of the shear-induced structures, we conducted a numerical analysis of rheological properties in a homogeneous solution based on the constitutive equation developed by Kaye-Bernstein, Kearsley, and Zapas (K-BKZ). In the low-to-intermediate shear rate $\dot{\gamma}$ region between τ_w^{-1} and τ_e^{-1}, where τ_w and τ_e are, respectively, terminal relaxation time and the relaxation time for chain stretching, the steady state rheological properties, such as shear stress σ and the first normal stress difference N_1, for the PS/DOP and PS/TCP solutions are found to be almost same and also well predicted by the K-BKZ equation, in spite of the fact that there is a significant difference in the shear-induced structures as observed by shear-SALS and shear-microscopy. This implies that the contribution of the concentration fluctuations built up by shear flow to the rheological properties seems very small in this $\dot{\gamma}$ region. On the other hand, once $\dot{\gamma}$ exceeds τ_e^{-1}, σ and N_1 for both PS/DOP and PS/TCP start to deviate from the predicted values. Moreover, when $\dot{\gamma}$ further increases and becomes higher than $\dot{\gamma}_{a,\mathrm{DOP}}$ (sufficiently higher than τ_e^{-1}), above which rheological and scattering anomalies are observed for PS/DOP, σ and N_1 for PS/DOP and PS/TCP are significantly larger than those predicted by K-BKZ. Particularly, a steep increase of σ and N_1 for PS/DOP above $\dot{\gamma}_{a,\mathrm{DOP}}$ is attributed to an excess free energy stored in the system via the deformation of interface of well-defined domains, which are aligned into the stringlike structure developed parallel to the flow axis, and stretching of the chains connecting the domains in the stringlike structures. Thus, we advocate that the effect of shear-induced structures should be well considered on the behavior of σ and N_1 at the high $\dot{\gamma}$ region above τ_e^{-1} in semidilute polymer solutions. © *2008 American Institute of Physics*. [DOI: 10.1063/1.2899662]

I. INTRODUCTION

When shear flow is imposed on a semidilute polymer solution in its one phase region, the solution often exhibits turbidity. This phenomenon is called shear-induced concentration fluctuations and/or phase separation, and many theoretical and experimental studies have been undertaken to understand this intriguing phenomenon.

Experimentally, the shear-induced concentration fluctuations and/or phase separation of the semidilute polymer solutions have been investigated mainly by light scattering[1–6] (LS) and/or small-angle neutron scattering (SANS).[7–9] We have studied the shear rate dependence of the structure factor of the semidilute polystyrene (PS)/dioctyl phthalate (DOP) solution in steady state and found that there are three characteristic shear rates, which will be discussed below in detail.[3,10]

Theoretically, Helfand and Fredrickson,[11] Milner,[12] and Onuki[13] (HFMO) have developed the dynamical equation of concentration fluctuations in the context of the time-dependent Ginzburg–Landau (TDGL) equation, which incorporates the gradient term of the stress tensor in order to explain this phenomenon. The addition of the gradient term of the stress tensor can express the effects of "dynamical coupling between stress and diffusion"[14] on the dynamics of concentration fluctuations in the systems comprised of constituent elements (polymer and solvent) having dynamically asymmetric properties.

In the one phase region of the systems, the thermal concentration fluctuations exist. Such concentration fluctuations generate the local variation of the stress field in the systems. This stress field, which is borne only by entangled polymers

a)Present Address, Japan Atomic Energy Agency, Advanced Science Research Center, Tokai-mura, Ibaraki 319-1195, Japan. Author to whom correspondence should be addressed. Electronic mail: hashimoto.takeji@jaea.go.jp and hashi2@pearl.ocn.ne.jp.

in the semidilute solutions to be dealt with here, influences the dynamics of concentration fluctuations through the free energy functional. Milner,[12] Ji and Helfand,[15] and Saito *et al.*[16] calculated the structure factor by using the linearized TDGL equation with the gradient term of the stress tensor in the context of the HFMO theory and found the increase in the structure factor under shear flow. The calculations indicate that the stress plays a major role on the shear-induced structures (i.e., concentration fluctuations and/or phase separation). We believe that it is important to understand how the shear-induced structures affect the rheological properties of the solutions as well as the dynamics of the structure factor of the solutions.

However, there are few rheological studies of the systems having well-characterized shear-induced concentration fluctuations and/or phase separation. Thus, in this paper, we shall investigate how the shear-induced concentration fluctuations and/or phase separation affect the viscoelastic behavior of the semidilute polymer solutions by using a simultaneous observation of rheology, shear-small-angle light scattering (shear-SALS), and shear-microscopy as a function of shear rate $\dot{\gamma}$. In particular, we shall focus on the steady state shear-induced structures and rheological properties.

In order to elucidate the above effects, we compared the shear stress σ and the first normal stress difference N_1 measured for the semidilute polymer solutions (having varying concentration fluctuations) with those calculated from the constitutive equation derived by Kaye-Bernstein, Kearsley, and Zapas (K-BKZ).[17,18] It is well known that the K-BKZ constitutive equation can phenomenologically describe the nonlinear viscoelastic behavior of homogeneous polymeric liquids and semidilute polymer solutions, particularly in the steady state.[19] In order to calculate the nonlinear viscoelastic response based on the K-BKZ equation, one needs fundamental data of linear viscoelasticity. The strain range used for the measurement of the linear viscoelasticity is much below the critical strain for the shear-induced concentration fluctuations and/or phase separation, so that the obtained linear viscoelasticity is surely the one for the homogeneous state. Thus, the nonlinear rheological properties calculated by using the K-BKZ equation can be regarded as the properties free from the effects of shear-induced structural change. The difference between the experimental results and the calculated values would certainly elucidate the effects of the shear-induced concentration fluctuations and/or phase separation on the nonlinear rheology.

In the following section, we will present a summary of the K-BKZ theory. The samples and the experimental techniques used in this study will be described in Sec. III. In Sec. IV A, we shall first show the rheological properties of the solutions. In Sec. IV B, we will present the shear rate dependence of the scattering structure factors and real space images, which characterize the shear-induced concentration fluctuations and/or phase separation. We shall discuss the relationship between the structure and rheological properties in Sec. V. Finally, in Sec. VI, we shall summarize our results.

II. BACKGROUND FOR THEORETICAL ANALYSIS

A. Numerical evaluation of σ and N_1 as a function of $\dot{\gamma}$ based on the K-BKZ-type constitutive equation

To calculate the rheological properties, we employed the separable K-BKZ-type constitutive equation[19] that has a mathematical formalism allowing the calculation of the stress tensor from a specified strain history. The separable K-BKZ constitutive equation has the following limitation: (i) It cannot predict the overshoot in the shear stress and the first normal stress difference after the onset of shear flow; (ii) the calculated steady state rheological behavior does not agree with the experimental results at higher shear rates where the chain stretching is believed to play an important role in the rheological behavior. Although there are these limitations in the K-BKZ equation, it is confirmed that K-BKZ can well predict the viscoelastic behavior such as shear thinning in steady state at low to moderate shear rates.[19–21] Thus, it is useful to compare the experimental data with the K-BKZ prediction.

From the K-BKZ equation, the time-dependent shear stress $\sigma(t;\gamma)$ and the first normal stress difference $N_1(t;\gamma)$ for the simple shear flow are given by

$$\sigma(t;\gamma) = \sigma_{xy} = \int_{-\infty}^{t} \sum_k \frac{G_k}{\tau_k} \exp\left(-\frac{t-t'}{\tau_k}\right) h(\gamma)\gamma dt', \tag{1}$$

$$N_1(t;\gamma) = \int_{-\infty}^{t} \sum_k \frac{G_k}{\tau_k} \exp\left(-\frac{t-t'}{\tau_k}\right) h(\gamma)\gamma^2 dt', \tag{2}$$

$$G(t) = \sum_i G_i \exp(-t/\tau_i), \tag{3}$$

where G_i and τ_i are, respectively, the relaxation intensity and the relaxation time of ith relaxation mode, describing shear modulus $G(t)$ in the linear viscoelastic regime, γ is a shear strain at a time t measured from the other time t' $(<t)$, and $h(\gamma)$ is the shear damping function. The shear stress and the first normal stress difference under steady shear flow can be calculated from the data of G_i and τ_i and damping function $h(\gamma)$.

In this study, we evaluated G_i and τ_i by fitting the data of real and imaginary parts of complex shear moduli, $G'(\omega)$ and $G''(\omega)$, respectively, with the following equations:

$$G'(\omega) = \sum_i G_i \frac{\omega^2\tau_i^2}{1+\omega^2\tau_i^2}, \tag{4}$$

$$G''(\omega) = \sum_i G_i \frac{\omega\tau_i}{1+\omega^2\tau_i^2}. \tag{5}$$

This fitting is equivalent to a fit of $G(t)$ data with Eq. (3). The details of the measurements of $G'(\omega)$ and $G''(\omega)$ will be described later in Sec. IV A. The best fitted $G'(\omega)$ and $G''(\omega)$ curves will be also shown, respectively, by solid and dotted lines later in Fig. 2.

The details of the linear viscoelastic properties of our system will be described later in Sec. IV A. The damping function $h(\gamma)$ characterizes the strain softening. In this study,

we utilize an empirical equation given below, which was previously obtained for tricresyl phosphate (TCP) solutions of PS from the same commercial batch,[22]

$$h(\gamma) = \frac{1}{1 + 0.2\gamma^2}. \quad (6)$$

The damping function [Eq. (6)] is almost universal in PS solutions, irrespective of the kind of solvents. Thus, only the linear viscoelastic data of our PS solutions are necessary for the calculation of the nonlinear behavior of the solutions by using Eqs. (1) and (2).

III. EXPERIMENTAL METHODS

A. Materials

We used semidilute polystyrene (PS) solutions. The PS sample, which was purchased from Toso Co., Ltd., had the weight average molecular weight of 5.48×10^6, and the heterogeneity index for the molecular weight distribution was 1.15. We chose DOP as a Θ solvent for PS (Θ temperature for PS is 22 °C) and TCP as a good solvent for PS. Both PS/DOP and PS/TCP have an upper-critical-solution-temperature-type phase diagram. The concentration of PS prepared was 6.0 wt%. The cloud point of PS/DOP at 6.0 wt% is 13.8 °C, while that of PS/TCP is below 0 °C. The c/c^* value is about 6.7 for PS/DOP and 7.4 for PS/TCP at 25 °C, where c^* is the overlap concentration determined in the previous paper.[23]

B. LS and optical microscopy

Simultaneous measurements of shear-SALS and shear-microscopy (SALS and optical microscopy) were carried out with the rheo-optical apparatus described elsewhere.[24] We applied the shear flow to the polymer solutions with the transparent cone-and-plate-type shear cell made of quartz with 80 mm diameter and 1° cone angle. By using a He–Ne laser having a wavelength of 632.8 nm in air as an incident beam source, we detected the two-dimensional LS pattern in the q_x-q_z plane with a charge-coupled device (CCD) camera, whose shutter speed was set to 10^{-4} s, as shown in Fig. 1(a). Here, q is the magnitude of the scattering vector $\mathbf{q}$ defined as $q = |\mathbf{q}| \equiv (4\pi/\lambda)\sin(\theta/2)$, where λ is the wavelength of the incident beam and θ is the scattering angle in the medium. The x-, y-, and z-axes are the flow, the velocity gradient, and the vorticity directions, respectively. The q_x, q_y, and q_z are the respective components of $\mathbf{q}$. The Cartesian coordinate is also shown in Fig. 1(a). In Fig. 1(b), we show the typical LS pattern in q_x-q_z plane after the onset of shear-induced concentration fluctuations and/or phase separation. The anisotropic two-dimensional scattering pattern with expanding two lobes of high intensity along the flow direction is called as a *butterfly pattern*. Due to the optical setup, q range for scattered light is limited inside the half circle with the radius of $q = 3.6 \times 10^{-3}$ nm^{-1}. The half circle corresponds to a window opened in the temperature enclosure for the SALS observation. The accessible q range is $6.3 \times 10^{-4} < q < 3.6 \times 10^{-3}$ nm^{-1}. The azimuthal angle μ is defined as the angle between the x-axis and $\mathbf{q}$. Snap shots of real space images

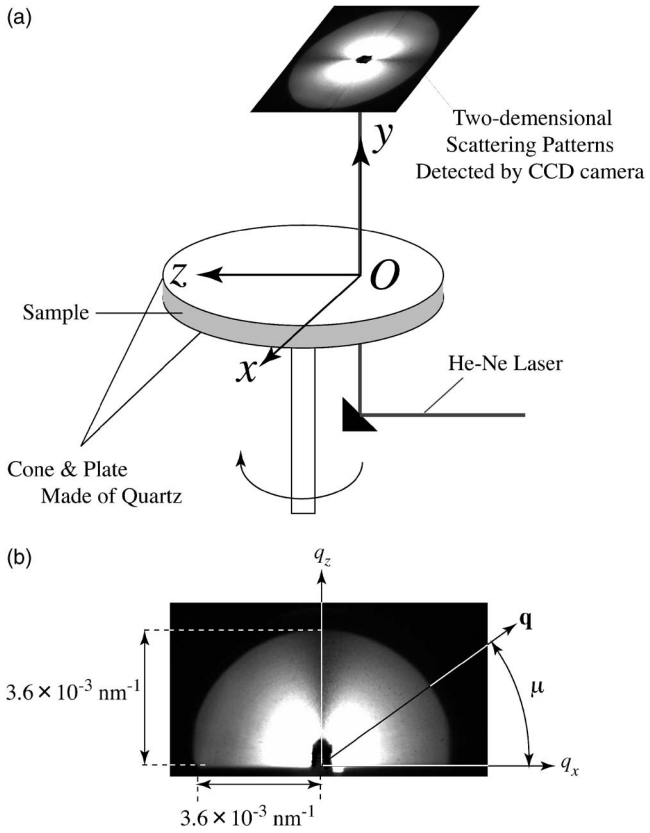

FIG. 1. (a) Definition of Cartesian coordinate and a schematic diagram of the SALS setup. The x-axis is parallel to the flow direction, the y-axis to the shear gradient direction, and the z-axis to the vorticity or neutral direction. The propagation of the incident beam is along the y-axis, and the 2D scattering pattern is detected on the q_x-q_z plane with a CCD camera. (b) The typical steady state butterfly pattern of PS/DOP 6.0 wt% at $T = 27$ °C and $\dot{\gamma} = 3.98$ s^{-1}, which belongs to the shear rate regime of $\dot{\gamma}_{cz} \leqslant \dot{\gamma} \leqslant \dot{\gamma}_a$, where $\dot{\gamma}_{cz}$ and $\dot{\gamma}_a$ will be defined later in Fig. 6.

were captured by a transmission optical microscope with a CCD camera. The measurement temperature was set at 27 °C, which is a little higher than the Θ point and much higher than the cloud point for the PS/DOP solution.

C. Viscoelastic measurements

We measured the storage modulus G' and the loss modulus G'', in a linear viscoelastic range, as well as steady state shear stress σ and first normal stress difference N_1 as a function of shear rate $\dot{\gamma}$ by using ARES-FS and RMS-800 (Rheometric Scientific Co. Ltd.) with a cone-plate fixture. The linear dynamic measurement was also made at 27 °C in the range of the angular frequency ω covered from 0.001 to 100 rad/s. The strain amplitude γ_0 used in this experiment was 0.2. Saito *et al.*[4] investigated the shear-induced enhancement of concentration fluctuations and/or phase separation under large amplitude oscillatory shear flow and constructed the phase diagram in the parameter space of γ_0 and ω for the same PS/DOP solution. The phase diagram shown in Fig. 5 in Ref. 4 indicates that the shear-induced enhancement of concentration fluctuations and/or phase separation does not occur at any ω if $\gamma_0 < 1$, so that the system behaves as a homogenous single-phase solution under the experimental condition for the linear dynamic

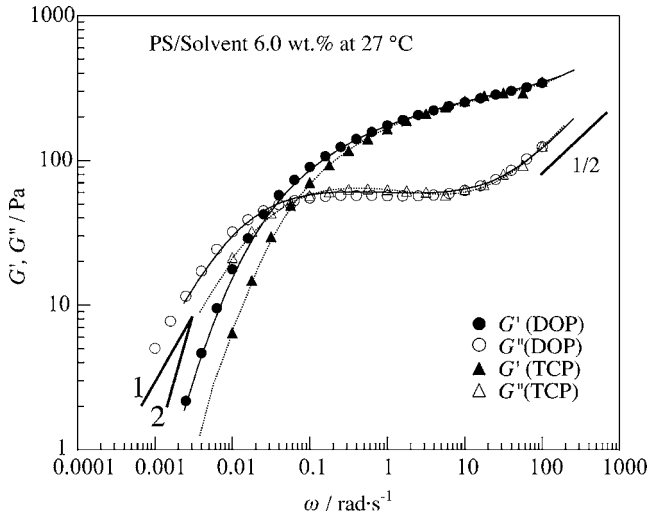

FIG. 2. Dynamic storage and loss moduli, $G'(\omega)$ (filled symbols) and $G''(\omega)$ (unfilled symbols), respectively, for PS/DOP (circles) and PS/TCP (triangles) solutions with a polymer concentration of 6.0 wt% at 27 °C. Strain amplitude γ_0 applied here was 0.2 where shear-enhanced concentration fluctuations is not observed (Ref. 4).

measurements. Although there are no reports about "shear-induced phase separation" in the PS/TCP systems under the oscillatory flow, it is quite unlikely that the oscillatory shear of $\gamma_0 < 1$ could induce any structural change in the PS/TCP systems as well. Hence, the linear viscoelasticity measured here exhibits that of the homogeneous solutions in the one phase region. In contrast, the shear rate dependence of the viscoelastic behavior under high shear represents the behavior of the solutions with some structural changes, which will be described in Sec. V B.

For the measurement of σ and N_1 in steady state, the simple shear flow was stepwisely imposed on the systems from zero shear rate to given rates without a gradual change in $\dot{\gamma}$ (we call this type of flow application as *shear jump*), and the systems were subjected to the flow for a sufficiently long time to attain steady state before the data acquisition.

IV. RESULTS

A. Linear viscoelasticity of PS/DOP and PS/TCP

G' and G'' for PS/DOP and PS/TCP at 27 °C as a function of ω are shown in Fig. 2. As already pointed out in Sec. III C, the shear-induced concentration fluctuations and/or phase separation does not occur under these measurement conditions. Thus, the solutions are homogeneous with equilibrium thermal concentration fluctuations in the one phase region. The terminal flow, rubbery plateau, and transition regions are observed for both solutions. However, the rubbery plateau region of PS/DOP is slightly wider than that of
PS/TCP, and the terminal flow region of PS/DOP shifts toward the lower ω region than that of PS/TCP, though the rubbery plateau modulus G_N of PS/DOP is identical with that of PS/TCP. Moreover, the transition region (high ω-regime) of them are well overlapped to each other. The difference between
PS/DOP and PS/TCP at the lower ω-regime indicates that the large length-scale response of entangled PS chains is affected by solvent quality: DOP is a Θ solvent but TCP is a good solvent for PS.[23]

As already reported by Inoue *et al.*,[25] this trend attributes to the effects of thermal concentration fluctuations in the one phase region. Since the temperature is close to the spinodal point for PS/DOP but far from the spinodal point for PS/TCP in the single-phase solution, the correlation length and the amplitude of the thermal concentration fluctuations are larger, and the dynamics of the thermal concentration fluctuations is slower in PS/DOP than that in PS/TCP. This factor may have affected the large length-scale motion and hence terminal relaxation of polymer chains, causing a shift of the terminal relaxation of PS/DOP toward lower ω compared to the case of PS/TCP. It should be noted that the thermal concentration fluctuations at equilibrium are different from those enhanced by shear. On the other hand, G' and G'' of PS/DOP are close to those of PS/TCP in the intermediate frequency region, which means that the local dynamics governing the relaxation at those ω appears to be the same for PS/DOP and PS/TCP, so that the local dynamics are independent of the amplitude of the concentration fluctuations, $\langle \Delta\phi^2 \rangle^{1/2}$. More detailed discussion will be given later in Sec. IV C and in the second paragraph of Sec. V A.

From Fig. 2, we can estimate two rheological characteristic parameters—the terminal linear viscoelastic relaxation time τ_w and the longest Rouse time τ_R of the solutions. These two parameters characterize (i) a fast process—relaxation time of molecular stretching with $\tau_e = 2\tau_R$—and (ii) a slow process—relaxation of molecular orientation with characteristic time τ_w. The longest Rouse time τ_R can be estimated by the method of Osaki *et al.*[26,27] Since we did not observe the power law behavior in G' over a wide range of ω, as shown in Fig. 2, τ_R was referred from the data evaluated by Osaki *et al.* for the same systems as we employed in this study: $\tau_R = 0.2$ s for the PS/DOP 6.0 wt% and PS/TCP 6.0 wt% solutions at 27.4 and 25.8 °C, respectively.[28] By neglecting a small difference between these temperature and our measurement temperature (27 °C), we may evaluate $\tau_e = 0.4$ s for both systems at 27 °C. τ_w is defined as $\tau_w \equiv [G'/\omega G'']_{\omega \to 0}$ and was estimated to be $\tau_w = 75$ and 33 s at 27 °C for PS/DOP and PS/TCP, respectively.

As already discussed in Sec. II, in order to calculate the steady state rheological behavior for the homogeneous semidilute solution with the K-BKZ constitutive equation, we obtained G_i and τ_i by fitting the measured data, $G'(\omega)$ and $G''(\omega)$ (shown by symbols in Fig. 2), to the functions described in Eqs. (4) and (5) (solid and broken lines in Fig. 2). As shown in Fig. 2, the fitting was excellently achieved with the least squares method to give G_i and τ_i used in the calculation. The set of parameters, G_i and τ_i, has as many numbers as the data points.

B. Results obtained by shear-SALS and shear-microscopy experiments

Figures 3 and 4, respectively, show the three-dimensional (3D) plots of linear-scaled relative LS intensity distribution in the q_x-q_z plane for PS/DOP and PS/TCP under

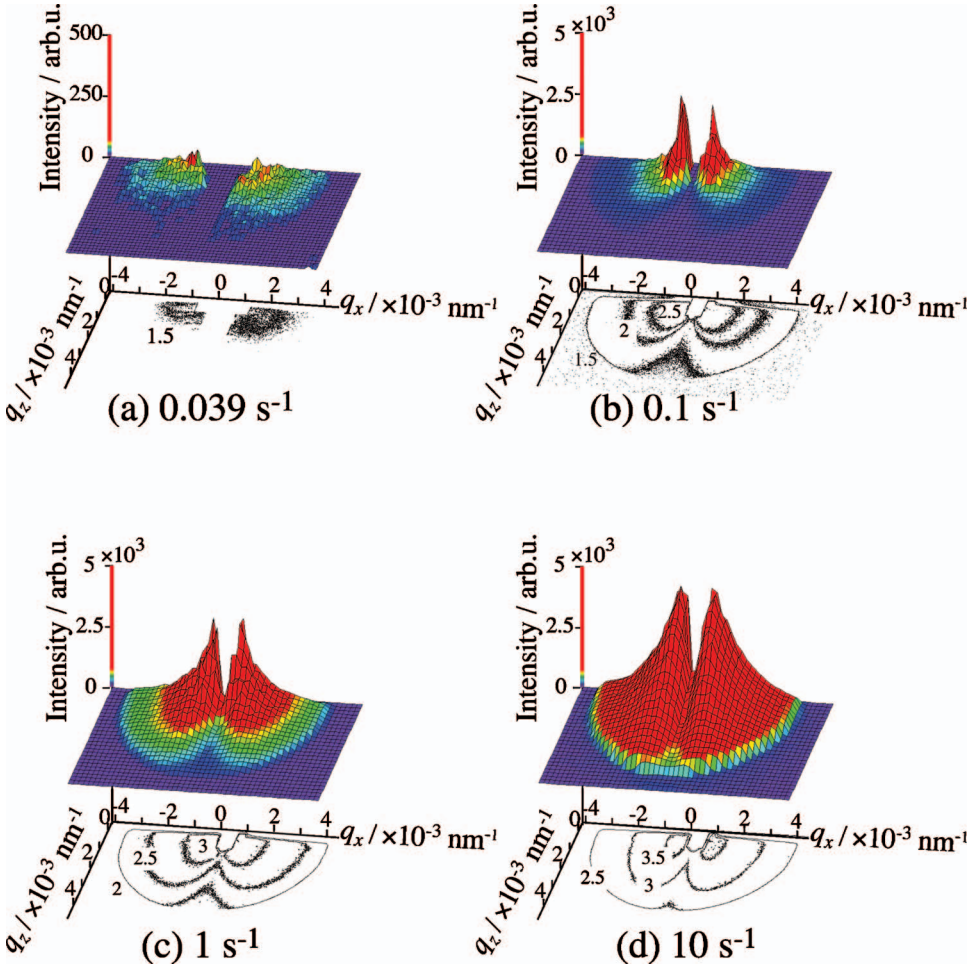

FIG. 3. (Color) 3D representation of steady state SALS intensity distributions at various shear rates for PS/DOP 6.0 wt% at 27 °C. The contour plots are also shown on the bottom of each 3D pattern and the labeled number on each contour line represents the logarithmic relative scattering intensity. Scattering intensity from DOP itself and electrical noise were subtracted as a background from the net scattering intensity. The relative intensity in parts (a)–(d) can be compared. A gradation was deliberately added to the intensity scale in order to facilitate an intuitive feeling of intensity distribution of the 3D patterns.

steady shear at $\dot{\gamma}$ as indicated. The logarithmic scale contour plots are also shown on the bottom of each 3D plot and the labeled numbers correspond to logarithmic relative scattered intensity levels. These 3D images of LS patterns help us to visualize the increase of intensities in the q_x-q_z plane with the shear. The relative intensity scale is common in parts (a)–(d) so that each pattern in Fig. 3 can be compared in terms of its relative intensity, and so as in Fig. 4. Each intensity distribution of PS/DOP can also be compared with that for PS/TCP when the refractive index difference of PS/DOP and PS/TCP is considered. The "canyon" between two peaks which corresponds to the "dark streak" in the LS pattern reported elsewhere[2,3] implies a relatively small increase of concentration fluctuations along the neutral direction.

The shear rate dependence of the transmission optical microscopic images for PS/DOP is shown in Fig. 5. The images of (a)–(d) correspond to scattering patterns (a)–(d) in Fig. 3 and reflect the shear-induced steady state structure at each shear rate. The spatial variations of the image contrast between dark and bright appear under shear flow and are enhanced with increasing $\dot{\gamma}$. The clear contrast can be observed at $\dot{\gamma}=10$ s^{-1}, indicating that the polymer-rich domains may be clearly created in the polymer poor matrix at $\dot{\gamma} \geqslant 0.1$ s^{-1}, even though the shear-induced structure is not a stringlike structure. The stringlike structure was observed at higher $\dot{\gamma}$.[29]

According to the LS results of PS/DOP at $\dot{\gamma}=0.1$ s^{-1}, the normalized integrated intensity along the x-axis is larger than 15 and that along the z-axis is larger than 1.5, as will be shown later in Fig. 6(a). This indicates that $\langle \Delta\phi^2 \rangle^{1/2}$ at this shear rate approximately becomes larger by about five times relative to that in quiescent state, as will be detailed in the Appendix. This in turn gives rise to an enhanced image contrast for the shear-induced structure, as shown in Fig. 5(b). In the case of PS/TCP, however, we were unable to observe the clear optical image even at the shear rate region, $0.2 \leqslant \dot{\gamma} \leqslant 3$ s^{-1}, where the normalized LS integrated intensity along the x-axis is ten times or more than that at quiescent state but that along the z-axis is unity. This is because the image contrast depends not only on $\langle \Delta\phi^2 \rangle^{1/2}$ but also on the refractive index difference Δn between polymer and solvent, though the normalized integrated intensity depends only on $\langle \Delta\phi^2 \rangle^{1/2}$, since the factor Δn is canceled out by the normalization process. Δn between PS and TCP is small ($|\Delta n| = |n_{\mathrm{TCP}} - n_{\mathrm{PS}}| = 0.045$) (Refs. 30 and 31) compared to that between PS and

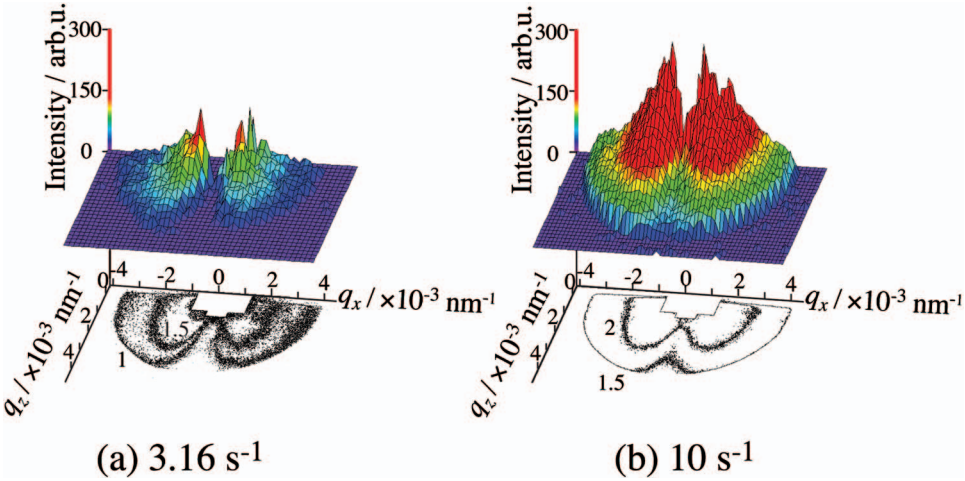

FIG. 4. (Color) 3D representation of steady state SALS intensity distributions at various shear rates for PS/TCP 6.0 wt% at 27 °C. The contour plots are also shown on the bottom of each 3D pattern and the labeled number on each contour line represents logarithmic relative scattering intensity. Scattering intensity from TCP itself and electrical noise were subtracted as a background from the net scattering intensity. The relative intensity in parts (a) and (b) can be compared to each other. It can also be compared with that in parts (a)–(d) in Fig. 3. The gradation added to the intensity scale was explained in Fig. 3.

DOP ($|\Delta n|=|n_{\mathrm{DOP}}-n_{\mathrm{PS}}|=0.11$).[30,31] Therefore, the large amplitude of concentration fluctuations attained for PS/TCP may not give enough contrast for the microscopy. In fact, we observed a heterogeneity in a microscopy image of PS/TCP only at a much higher shear rate ($\dot{\gamma}\geqslant 50$ s^{-1}).

In order to characterize the shear rate dependence of the shear-induced concentration fluctuations and/or phase separation, we have investigated the shear rate dependent integrated intensities as

$$\mathcal{I}_x(\dot{\gamma}) = \int_{q_{x,\min}}^{q_{x,\max}} I(q_x;\dot{\gamma})dq_x, \tag{7}$$

$$\mathcal{I}_z(\dot{\gamma}) = \int_{q_{z,\min}}^{q_{z,\max}} I(q_z;\dot{\gamma})dq_z, \tag{8}$$

where $q_{x,\min}$ and $q_{x,\max}$ are the lower and upper limits of the experimental q window along q_x, and the same for $q_{z,\min}$ and $q_{z,\max}$. Figures 6(a) and 6(b), respectively, show normalized integrated intensities along q_x, $\mathcal{I}_x(\dot{\gamma})/\mathcal{I}_x(0)$ and q_z, $\mathcal{I}_z(\dot{\gamma})/\mathcal{I}_z(0)$ as a function of $\dot{\gamma}$ for PS/DOP and PS/TCP, respectively, at 27 °C. Here, $\mathcal{I}_x(0)$ and $\mathcal{I}_z(0)$ are, respectively, $\mathcal{I}_x(\dot{\gamma})$ and $\mathcal{I}_z(\dot{\gamma})$ at $\dot{\gamma}=0$ s^{-1}.

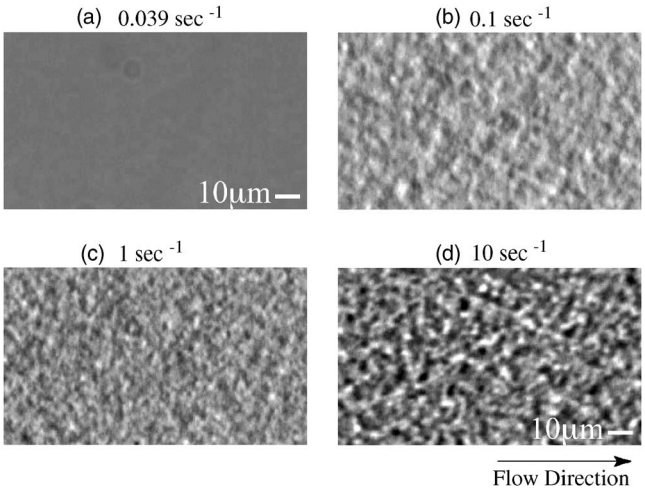

FIG. 5. Transmission optical microscopic images at various shear rates for PS/DOP at 27 °C. The annotations correspond to those of in Fig. 3.

As we have reported elsewhere,[3,10] the three critical shear rates, $\dot{\gamma}_{cx}$, $\dot{\gamma}_{cz}$, and $\dot{\gamma}_a$ with increasing order of $\dot{\gamma}$ are defined regarding the shear-enhanced concentration fluctuations or shear-induced structure formation. They are determined from the shear rate dependence of $\mathcal{I}_x(\dot{\gamma})$ and $\mathcal{I}_z(\dot{\gamma})$.

$\dot{\gamma}_{cx}$ is the shear rate, where $\mathcal{I}_x(\dot{\gamma})/\mathcal{I}_x(0)$ starts to increase with $\dot{\gamma}$ while $\mathcal{I}_z(\dot{\gamma})/\mathcal{I}_z(0)$ does not yet increase in the SALS experimental q window, indicating that the shear-enhanced concentration fluctuations are brought about by the shear flow along the flow direction. The values of $\dot{\gamma}_{cx}$ are 0.03 s^{-1} for PS/DOP and 0.06 s^{-1} for PS/TCP, which are close to their terminal relaxation frequency τ_w^{-1} (0.013 and 0.03 s^{-1}, respectively). At $\dot{\gamma}>\dot{\gamma}_{cx}$, a butterfly pattern, as shown in Figs. 3 and 4, appears with a dark streak perpendicular to flow. Its wings expand toward a large value of azimuthal angel μ and hence the dark streak narrows around the z-axis with increasing $\dot{\gamma}$.

$\dot{\gamma}_{cz}$ is the shear rate, where $\mathcal{I}_z(\dot{\gamma})/\mathcal{I}_z(0)$ starts to increase. This indicates that the concentration fluctuations also appear along the z-axis. The values of $\dot{\gamma}_{cz}$ are 0.07 s^{-1} for PS/DOP and 3 s^{-1} for PS/TCP. The solvent quality of DOP and TCP to PS is quite different; thus, $\dot{\gamma}_{cz}$ of PS/DOP and PS/TCP appears in quite different shear rate regions, i.e., below τ_e^{-1} for PS/DOP while above τ_e^{-1} for PS/TCP (τ_e=0.4 s for both systems). The detailed discussion about solvent quality dependence of these critical shear rates is given in Ref. 23. At $\dot{\gamma}>\dot{\gamma}_{cz}$, the butterfly wings still become wider along the μ direction because the Fourier modes of concentration fluctuations with their wave vectors at larger μ still grow with an increase in $\dot{\gamma}$.

$\dot{\gamma}_a$ shown in Fig. 6(a) is critical shear rate above which the following types of anomalous behavior are observed both in SALS and rheology experiments: With increasing $\dot{\gamma}$ above $\dot{\gamma}_a$, $\mathcal{I}_x(\dot{\gamma})/\mathcal{I}_x(0)$ and $\mathcal{I}_z(\dot{\gamma})/\mathcal{I}_z(0)$ further increase [as shown in Fig. 6(a)]; σ and N_1 exhibit shear thickening, as will be

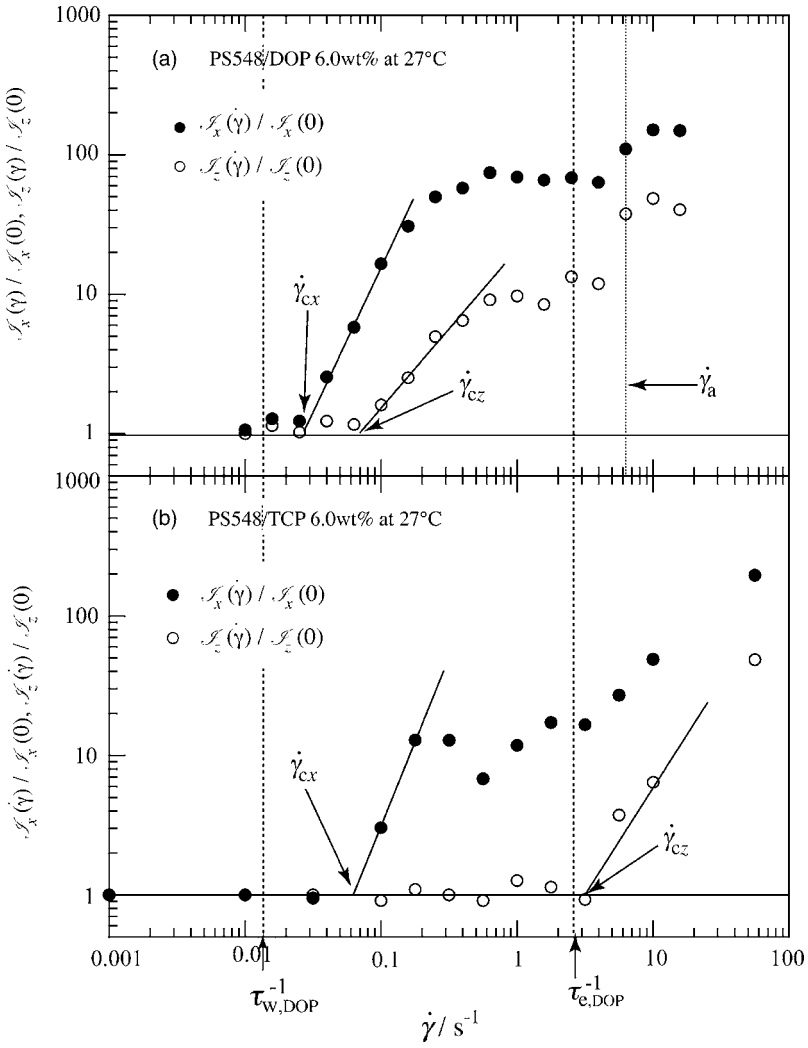

FIG. 6. Normalized integrated intensities $\mathcal{I}_x(\dot\gamma)/\mathcal{I}_x(0)$ and $\mathcal{I}_z(\dot\gamma)/\mathcal{I}_z(0)$ as a function of shear rate $\dot\gamma$ in double logarithmic scale for (a) PS/DOP 6.0 wt% at 27 °C and (b) PS/TCP 6.0 wt% at 27 °C. Critical shear rates $\dot\gamma_{cx}$ and $\dot\gamma_{cz}$ are, respectively, determined as the value at which the two straight lines fitted to the data points of $\mathcal{I}_x(\dot\gamma)/\mathcal{I}_x(0)$ and $\mathcal{I}_z(\dot\gamma)/\mathcal{I}_z(0)$ intersect, as shown in the figure. $\dot\gamma_a$ is determined as the shear rate at which both normalized integrated intensities start to increase again with a further increase of $\dot\gamma$ above $\dot\gamma_{cz}$. $\dot\gamma_a$ for PS/TCP is not explicitly observed in this experimental shear-rate region.

shown later in Figs. 7 and 8. The increase of $\mathcal{I}_z(\dot\gamma)/\mathcal{I}_z(0)$ above $\dot\gamma_a$ is related to the appearance of a sharp streaklike scattering extended along q_z above $\dot\gamma_a$. In Fig. 3(d), the streaklike scattering is evidenced by the disappearance of the canyon between the two peaks of the butterfly wings or the disappearance of the dark streak in the butterfly pattern along q_z. The sharp streaklike scattering becomes more remarkable and self-evident at higher shear rates (e.g., $\dot\gamma$=50 s^{-1}) for the same PS/DOP solution at the same temperature, as already reported in Fig. 12(d) of Ref. 29 and Fig. 7 of Ref. 32. Furthermore, the combined shear-SALS and shear-microscopy studies[32] revealed that the sharp streaklike scattering is due to the formation of stringlike structures parallel to the flow direction in which polymer-rich domains aligned parallel to the string axis. The model for the stringlike structure was proposed in our previous publications (see Fig. 8 in Refs. 29 and 32). We proposed[32] that (i) the stringlike structure as a whole gives rise to the streaklike scattering and (ii) the polymer-rich domains as an internal structure of the stringlike structure gives rise to the butterfly-type scattering patterns superposed on the streaklike scattering pattern. Although not explicitly stated in the previous reports,[29,32] we may propose that the domains in the stringlike structure are interconnected with highly stretched chains oriented along the flow direction, as evidenced by a dramatic increase in the negative value of birefringence[39] at high $\dot\gamma$ in parallel to the clear-cut appearance of the streaklike scattering, stringlike structures, and shear thickening.

$\dot\gamma_a$ is estimated as 7 s^{-1} for PS/DOP. On the other hand, for PS/TCP, $\dot\gamma_a$ is not clearly estimated by SALS experiment. However, we inferred from rheology experiment that $\dot\gamma_a$ may exist between 32 and 56 s^{-1}.[33] These critical shear rates are also summarized in Table I together with another rheological characteristic times.

C. Comparison between rheology experiment and K-BKZ calculation in low-to-intermediate shear rate region

The shear rate dependence of σ and N_1 of PS/DOP and PS/TCP are shown in Figs. 7(a) and 7(b), respectively. The solid and dotted lines show the K-BKZ calculation results for PS/DOP and PS/TCP, respectively. As described in Sec. II, it is important to note here again that the separable K-BKZ constitutive equation utilizing the $h(\gamma)$ data cannot describe at the high shear rate region where nonlinear effects due to the chain stretching dominate the viscoelastic behavior. Thus, we compared the experiment and the calculation only at $\dot\gamma < \tau_e^{-1}$ (=3 s^{-1}).

In Fig. 7, we first note that the σ and N_1 data for the

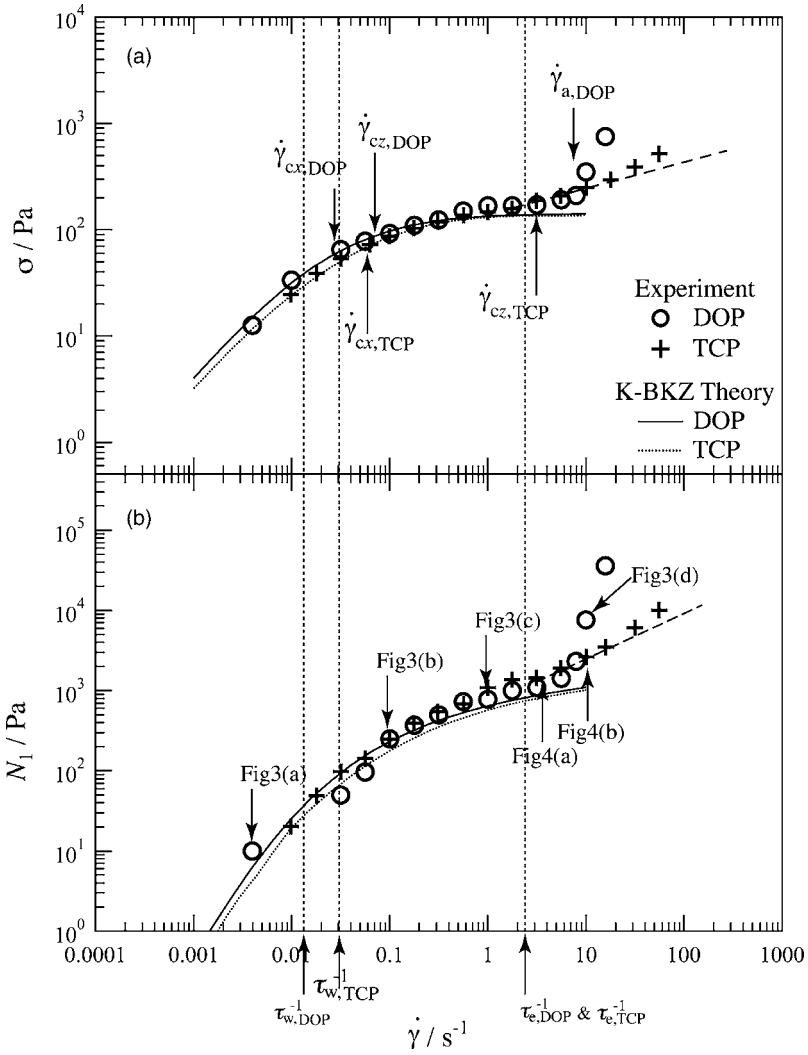

FIG. 7. (a) Steady state shear stress σ and (b) first normal stress difference N_1 as a function of share rate $\dot{\gamma}$ in double logarithmic scale. Unfilled circles and cross symbols indicate PS/DOP and PS/TCP data, respectively, while solid and dotted lines indicate the calculated data for PS/DOP and PS/TCP using Eqs. (1) and (2) in the text, respectively. The annotation, Fig. $X(i)$, in part (b), where $X=3$ or 4 and $i=a$, b, c, or d represents the figure number Fig. $X(i)$ showing the shear-SALS patterns characteristic for each sheared solution. The significant increase of σ and N_1 for PS/DOP above $\dot{\gamma}=10$ s^{-1} indicates a trend of the formation for the string-like structure in the PS/DOP solution. The broken lines are drawn by extrapolating from the data points in the intermediate shear region with straight lines.

PS/DOP solution at $\dot{\gamma}<0.03$ s^{-1} ($=\tau_{w,TCP}^{-1}$) are slightly different from the PS/TCP solution. At $\dot{\gamma}<0.03$ s^{-1}, the solutions are almost in the linear regime where $\sigma \propto \dot{\gamma}$ and $N_1 \propto \dot{\gamma}^2$ [and the K-BKZ calculation agrees with the linear calculation with $h(\gamma)=1$], and this difference merely reflects a discrepancy in their slow relaxation behavior seen for G' and G'' data, as already described above in Sec. IV A.

More importantly, σ and N_1 in the intermediate shear rate region, 0.03 s$^{-1}<\dot{\gamma}<3$ s^{-1} ($\tau_{w,TCP}^{-1}<\dot{\gamma}<\tau_e^{-1}$), are almost identical for the two solutions, and the K-BKZ calculation results fall well onto the experimental results. This is an intriguing and striking result. It unequivocally indicates that the viscoelastic behavior is not affected by the shear-induced structures in this shear rate region, irrespective of the fact that the amplitude of concentration fluctuations is significantly different for the two systems, for example, by a fact of about 7 at $\dot{\gamma}=1$ s^{-1} [see Figs. 3 and 4 as well as Figs. 6(a) and 6(b); see also the Appendix]. The reason why the rheological behavior is insensitive to the shear-enhanced local concentration fluctuations may be attributed to the fact that the shear-induced structures and the interface of structures have not yet well developed in this shear rate region. More detailed discussion will be given later in Sec. V A (in the second paragraph).

The experimentally observed increase of σ and N_1 for both PS/DOP and PS/TCP above $\dot{\gamma}_{a,DOP}$ clearly indicates a consequence of the formation of a new shear-induced structure, as will be discussed in more detail in Sec. V B.

V. DISCUSSION

A. Comparison of viscoelastic behavior of PS/DOP and PS/TCP in the low-to-intermediate shear rate region

The discrepancy in steady state σ and N_1 of PS/DOP and PS/TCP at $\dot{\gamma}<0.03$ s^{-1} (linear regime) reflects the difference of the terminal relaxation time τ_w between PS/DOP and PS/TCP, which is in turn attributed to the effects of the thermal concentration fluctuations at equilibrium. As already pointed out by Inoue *et al.*,[25] the motion of the whole chain governing σ and N_1 at these $\dot{\gamma}$ is cooperative, so that the mobility of the whole chain is controlled by the friction in the highest concentration regime. Thus, the motion of the whole chain is slower in PS/DOP than that in PS/TCP since the amplitude and the wavelength of the thermal concentration fluctuations are larger in PS/DOP than those in PS/TCP.

To our interest at $\tau_{w,TCP}^{-1} \leqslant \dot{\gamma} \leqslant \tau_{e,TCP}^{-1}$ (or $\tau_{e,DOP}^{-1}$), the steady state σ and N_1 for PS/DOP and PS/TCP well agree with each other and also with the calculated results, although the local concentration fluctuations brought about by the

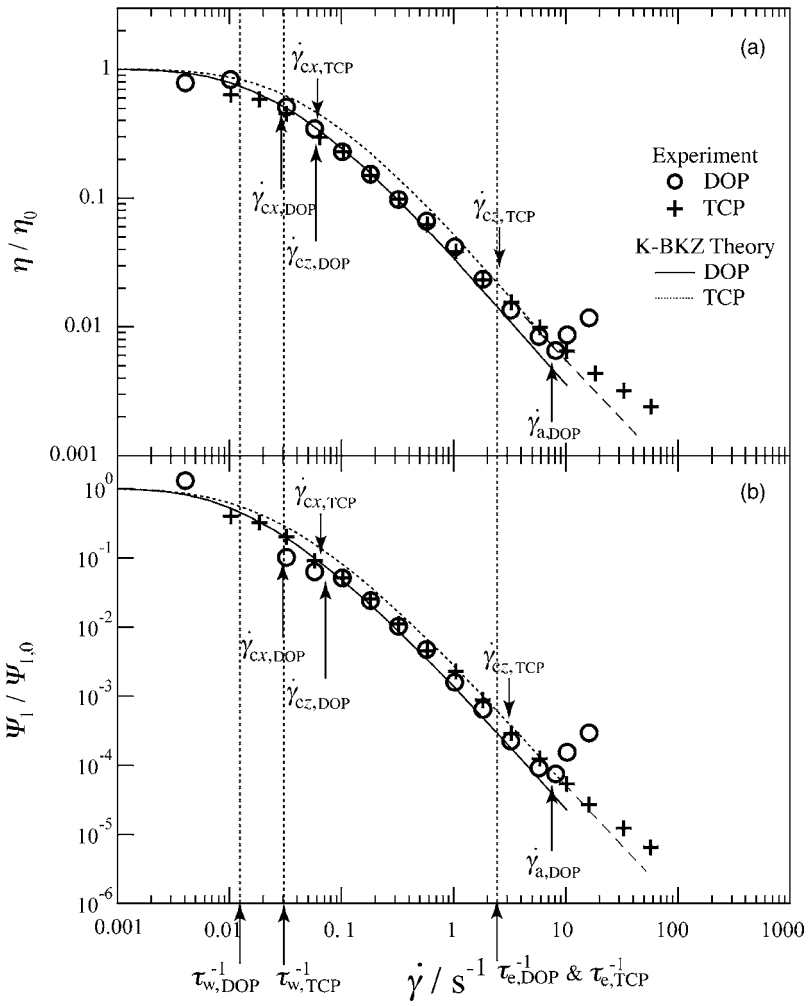

FIG. 8. (a) Steady state normalized shear viscosity η/η_0 and (b) normalized first normal stress coefficient $\Psi_1/\Psi_{1,0}$ as a function of shear rate $\dot{\gamma}$ in double logarithmic scale for PS/DOP and PS/TCP solutions with 6.0 wt% at 27 °C. Unfilled circles and cross symbols indicate PS/DOP and PS/TCP data, respectively, and solid and dotted lines indicate the calculated data for PS/DOP and PS/TCP using Eqs. (1) and (2) in the text, respectively. The broken line on PS/TCP above $\dot{\gamma}_a$ has the same meaning, as appeared in Fig. 7.

flow are different between PS/DOP and PS/TCP. We can make a rough estimate of the difference as follows: The fact that $[\mathscr{I}_x(\dot{\gamma})/\mathscr{I}_x(0)][\mathscr{I}_z(\dot{\gamma})/\mathscr{I}_z(0)]$ for PS/DOP is fifty times larger than that for PS/TCP represents that the amplitude of concentration fluctuations $\langle \Delta\phi^2 \rangle^{1/2}$ for PS/DOP is larger than that for PS/TCP by about seven times, as will be detailed in the Appendix. The viscoelastic properties seem insensitive to the shear-induced structures. The stress, which is associated with the excess free energy per unit volume generated by flow, depends on ΔF_{os} and ΔF_{ve}, where ΔF_{os} is osmotic energy per unit volume required to create the concentration fluctuations (or shear-induced structures) and ΔF_{ve} is the viscoelastic energy per unit volume required to create orientation of entangled chains. The insensitivity may infer $\Delta F_{os} < \Delta F_{ve}$. Here, ΔF_{os} has the order of $k_B T \Lambda^{-3}$, where Λ is the characteristic length of shear-induced structures. When Λ is in the order of micron meters as detected by the shear-SALS experiments, ΔF_{os} may become quite small compared to ΔF_{ve}, which is in the order of $k_B T N_{ent}$, where N_{ent} is the number density of elastically active network strand (entanglement segment). N_{ent} is an average over the regions rich and poor in polymers in the case when the shear-induced structures exist. If N_{ent} is invariant of the shear-induced structures for the range of $\tau_{w,TCP}^{-1} < \dot{\gamma} < \tau_e^{-1}$, the shear-induced structures have negligible effects on the nonlinear viscoelasticity. The same explanation can be applied to the agreement between the experimental and the calculated results with the separable K-BKZ constitutive equation.

B. Comparison of viscoelastic behavior of PS/DOP and PS/TCP in high shear rate region

We shall now focus on the rheological behavior of PS/DOP and PS/TCP measured at the high shear rate region,

TABLE I. Characteristic shear rate and relaxation rate or time of PS/DOP 6.0 wt% at 27 °C.

	$\dot{\gamma}_{cx}$ (s^{-1})	$\dot{\gamma}_{cz}$ (s^{-1})	$\dot{\gamma}_a$ (s^{-1})	$(\tau_w)^{-1}$ (s^{-1})	$(\tau_e)^{-1}$[a] (s^{-1})	τ_w (s)	τ_R (s)
PS/DOP	0.03	0.07	7	0.013	2.5	75	0.2
PS/TCP	0.06	3	32–56[b]	0.03	2.5	33	0.2

[a] $(\tau_e)^{-1} = (2\tau_R)^{-1}$.
[b] $\dot{\gamma}_a$ of PS–TCP is not clearly estimated by SALS experiment. However, we inferred from rheology experiment that $\dot{\gamma}_a$ may exist between 32 and 56 s^{-1} (Ref. 33).

$\dot{\gamma} > \dot{\gamma}_{a,\mathrm{DOP}}$. In this regime, the increase of σ and N_1 beyond the values expected from the data points in the intermediate shear rate region (as shown by the broken straight line extrapolated by using the data points in the intermediate shear region) is observed in both solutions. This trend is also observed by other researchers[34–36] and theoretically predicted as a result of tube and chain stretching for entangled polymer systems.[36–38] However, we attribute this resulted increase of σ and N_1 not only to the chain stretching but also to the structure constructed by flow. In fact, the magnitude of increase in σ and N_1 for PS/DOP is much larger than that of PS/TCP, as seen in Fig. 7. Moreover, σ and N_1 smoothly increase with increasing $\dot{\gamma}$ across $\dot{\gamma}_{a,\mathrm{DOP}}$ in the case of PS/TCP, while σ and N_1 for PS/DOP abruptly increase or are bent at the point of $\dot{\gamma} = \dot{\gamma}_a$. The drastic increases in the scattering intensity as well as in σ and N_1 for PS/DOP indicate that the phase-separated structure is developed to result in the formation of a stringlike structure at higher $\dot{\gamma}$. It should also be noted that the drastic decrease of birefringence from 0 to the large negative value above $\dot{\gamma}_a$ was observed for PS/DOP systems, indicating a dramatic increase of molecular orientation of PS parallel to the flow direction due to a strong chain stretching.[39] Therefore, ΔF_{ve} dramatically increases in PS/DOP.

It is conceivable that the phase-separated structures have more or less well-developed interface, as revealed by SANS studies by Morfin *et al.*[8] and Saito *et al.*[9] Although the studies were conducted for the PS/DOP systems having a different molecular weight of PS, a polymer concentration, and temperature, the SANS scattering profiles $I(q)$ at the high shear rates (but slightly smaller than $\dot{\gamma}_{a,\mathrm{DOP}}$) were represented by a weighted sum of the Ornstein–Zernicke (OZ) scattering function having the thermal correlation distance of ~10 nm and squared Lorentzian (SQL) or modified squared Lorentzian (m-SQL) function with the characteristic exponent n close to zero and the domain correlation distance of ~300 nm. Here, OZ is the scattering due to thermal concentration fluctuations of polymer chains, while SQL or m-SQL with the small value of n is the scattering due to domain structures with a more or less sharp interface. When $\dot{\gamma}$ is further increased above $\dot{\gamma}_a$, it is well expected that the domains aligned parallel to the axis of the stringlike structure have an increasingly well-defined interface and are interconnected by bundles of highly stretched chains oriented along the flow direction.[40]

On the other hand, PS/TCP may not yet have the fully phase-separated structures in this shear rate region, though the notable increase of the LS intensity is observed in this region. This may indicate a trend of the stringlike structure formation. Thus, the increase of ΔF_{ve} is less remarkable than the case of PS/DOP in the same shear rate region between $\dot{\gamma}_{a,\mathrm{DOP}}$ and 50 s^{-1}. The increase in σ and N_1 for PS/TCP are considered to be mainly due to the chain stretching, which is moderate compared to the case of PS/DOP.

We extend the above considerations to interpretations of the results shown in Fig. 8. The shear rate dependence of normalized viscosity η/η_0 and first normal stress coefficient $\Psi_1/\Psi_{1,0}$ are shown in Figs. 8(a) and 8(b), respectively, where η_0 and $\Psi_{1,0}$ are the zero shear values of viscosity and first normal stress coefficient. The significant shear thinning known as one of the nonlinear viscoelastic effects appears in the intermediate shear rate region, $\tau_w^{-1} < \dot{\gamma} < \tau_e^{-1}$, for both PS/DOP and PS/TCP. Since this behavior of η/η_0 and $\Psi_1/\Psi_{1,0}$ at these $\dot{\gamma}$ is well described by the K-BKZ calculation (the solid and dotted lines), the shear thinning of both PS/DOP and PS/TCP is dominantly accompanied by chain orientation and relaxation.

However, the shear thickening clearly appears at $\dot{\gamma} > \dot{\gamma}_{a,\mathrm{DOP}}$ in PS/DOP, which indicates a strong deviation from the K-BKZ prediction. We attribute this thickening of PS/DOP not only to ΔF_{ve} due to the chain orientation and ΔF_{os} but also to a significant contribution of excess free energy arising from the interfacial energy due to the formation of "domain interface" and from bundles of stretched chains connecting the domains within the stringlike structure.

On the contrary to the case of the PS/DOP solution, the PS/TCP solution only shows shear thinning in the same shear rate range, where the PS/DOP solution shows the shear thickening. However, a close observation shows that slopes of $\log(\eta/\eta_0)$ versus $\log\dot{\gamma}$ and $\log(\Psi_1/\Psi_{1,0})$ versus $\log\dot{\gamma}$ change upon increasing $\dot{\gamma}$ above about 30 s^{-1}, as demonstrated by the deviations of the data points from the broken line in Fig. 8. This is primarily the result of the chain stretching as already described above and also may be an indication of a tendency toward the shear thickening and formation of the stringlike structures in the PS/TCP solutions as well. We have not yet prove the existence of the interface of the domains comprising the string, since we have not yet conducted SANS studies for the PS/TCP solutions above $\dot{\gamma} > 30$ s^{-1}. These studies deserve a future work.

VI. SUMMARY

We aimed to elucidate the effects of shear-enhanced concentration fluctuations and/or shear-induced structure formation on the steady state viscoelastic properties of the entangled polymer solutions. In order to compare the steady state viscoelastic behavior between the solutions having shear-induced concentration fluctuations and/or phase separation and those of homogeneous solution, we calculated the shear stress σ and the normal stress differences N_1 by using the K-BKZ-type constitutive equation as those representing the homogeneous solutions and compared the calculated results with the experimental results on σ and N_1 for the solutions having well-characterized concentration fluctuations by means of shear-SALS and shear-microscopy. The deviation of measured σ and N_1 from those predicted was not observed at all in the shear rate region between τ_w^{-1} and τ_e^{-1}. This means that the contribution of shear-enhanced concentration fluctuations is surprisingly small, though the amplitude of the local concentration fluctuations in the solutions is large. Therefore, the viscoelastic energy ΔF_{ve} stored in the oriented chains overwhelms the stress tensor.

On the other hand, once the shear rate became higher than τ_e^{-1}, specifically greater than $\dot{\gamma}_a$, the anomalous increase of LS intensity was followed by the rheological anomaly. The rheological anomaly was discerned from a steep increase of the slope in $\log\sigma$ versus $\log\dot{\gamma}$ and $\log N_1$

versus log $\dot{\gamma}$ or log(η/η_0) versus log $\dot{\gamma}$ and log($\Psi_1/\Psi_{1,0}$) versus log $\dot{\gamma}$. This anomaly corresponds to the onset of shear thickening. We attributed this significant change in the viscoelastic behavior, especially remarkable in PS/DOP, to the shear-induced formation of the stringlike structure comprising series of domains, which have a well-developed interface aligned and interconnected along the string axis by bundles of strongly stretched chains. Once the clear stringlike structure is created, the excess free energy stored in the solutions significantly increases due to an increase of the interfacial energy via the formation of the domain interface and to an increase of elastic energy via strongly stretched chains, which connect the domains together in the stringlike structure. Thus, we would like to bring attention to the possible effect of shear-induced structure on the anomalous nonlinear rheological behavior, such as the shear thickening, appeared in semidilute polymer solutions at the high shear rate region.

APPENDIX: ESTIMATION OF $\langle \Delta\phi^2(\dot{\gamma})\rangle_{DOP}/\langle \Delta\phi^2(\dot{\gamma})\rangle_{TCP}$

Light scattering intensity $I(q)$ is given by Fourier transformation of the correlation function $g(\mathbf{r})$ for spatial refractive index fluctuations in the solutions,

$$I(\mathbf{q}) = K\langle \eta^2\rangle \int_0^\infty g(\mathbf{r})\exp[-i(\mathbf{q}\cdot\mathbf{r})]d\mathbf{r}, \tag{A1}$$

where K is a proportionality constant independent of q. $\langle \eta^2\rangle$ is the mean-squared refractive index fluctuation, which is proportional to the mean-squared local concentration fluctuations $\langle \Delta\phi^2\rangle$. $\langle \eta^2\rangle$ is estimated from an invariant Q,

$$\langle \eta^2\rangle \propto \langle \Delta\phi^2\rangle \propto Q = \int I(\mathbf{q})d\mathbf{q}, \tag{A2}$$

where the integration is carried out over the whole q space.

To estimate $\langle \eta^2\rangle$ for an anisotropic system like a sheared system, 3D distribution of $I(\mathbf{q})$ over the whole q space is required to obtain. However, we only measured $I(\mathbf{q})$ in the q_x-q_z plane due to the limitation of the apparatus. LS experiments carried out by other researchers[41,42] show that PS/DOP subjected to continuous shear flow at high shear rates exhibits the butterfly pattern in the q_x-q_y plane approximately similar to that obtained in the q_x-q_z plane. Thereupon, we assume that the butterfly patterns developed at the shear rates of our interest have the cylindrically symmetric intensity distribution around the x-axis in order to assess a rough order estimation of the ratio of $\langle \Delta\phi^2\rangle$ for PS/DOP, $\langle \Delta\phi^2\rangle_{DOP}$, to $\langle \Delta\phi^2\rangle$ for PS/TCP, $\langle \Delta\phi^2\rangle_{TCP}$. Then, $I(\mathbf{q})$ is described as

$$I(\mathbf{q}) = I(q_x, q_\perp) \cong I(q_x)I(q_\perp), \tag{A3}$$

where $q_\perp$ is a component of $\mathbf{q}$ perpendicular to the x-axis.

Now, we obtained from Eq. (A2),

$$\begin{aligned}\langle \Delta\phi^2\rangle &\propto \int\int I(q_x,q_\perp)dq_x 2\pi q_\perp dq_\perp \\ &\cong \int I(q_x)dq_x \int I(q_\perp)2\pi q_\perp dq_\perp \\ &= \mathscr{I}_x(\dot{\gamma})\int I(q_\perp)2\pi q_\perp dq_\perp \equiv \mathscr{I}_x(\dot{\gamma})\mathscr{I}_\perp(\dot{\gamma}).\end{aligned} \tag{A4}$$

Herewith, the normalized integrated intensities along q_x and $q_\perp$, $\mathscr{I}_x(\dot{\gamma})/\mathscr{I}_x(0)$ and $\mathscr{I}_\perp(\dot{\gamma})/\mathscr{I}_\perp(0)$, respectively, enable us to compare $\langle \Delta\phi^2(\dot{\gamma})\rangle$ for PS/DOP and PS/TCP at a given $\dot{\gamma}$,

$$\langle \Delta\phi^2(\dot{\gamma})\rangle/\langle \Delta\phi^2(0)\rangle = \mathscr{I}_x(\dot{\gamma})\mathscr{I}_\perp(\dot{\gamma})/\mathscr{I}_x(0)\mathscr{I}_\perp(0). \tag{A5}$$

At $\dot{\gamma}=1\ s^{-1}$, the ratio of $\langle \Delta\phi^2\rangle$ for PS/DOP and PS/TCP is estimated as follows:

$$\frac{\langle \Delta\phi^2(\dot{\gamma})\rangle_{DOP}}{\langle \Delta\phi^2(\dot{\gamma})\rangle_{TCP}} = \frac{\langle \Delta\phi^2(0)\rangle_{DOP}}{\langle \Delta\phi^2(0)\rangle_{TCP}}\left[\frac{\mathscr{I}_x(\dot{\gamma})}{\mathscr{I}_x(0)}\frac{\mathscr{I}_\perp(\dot{\gamma})}{\mathscr{I}_\perp(0)}\right]_{DOP}\Bigg/\left[\frac{\mathscr{I}_x(\dot{\gamma})}{\mathscr{I}_x(0)}\frac{\mathscr{I}_\perp(\dot{\gamma})}{\mathscr{I}_\perp(0)}\right]_{TCP}, \tag{A6}$$

$$= \frac{50\langle \Delta\phi^2(0)\rangle_{DOP}}{\langle \Delta\phi^2(0)\rangle_{TCP}}, \tag{A7}$$

since at $\dot{\gamma}=1\ s^{-1}$, $[\mathscr{I}_x(\dot{\gamma})/\mathscr{I}_x(0)]_{DOP}\cong 60$ and $[\mathscr{I}_x(\dot{\gamma})/\mathscr{I}_x(0)]_{TCP}\cong 12$ are found and $[\mathscr{I}_\perp(\dot{\gamma})/\mathscr{I}_\perp(0)]_{DOP}/[\mathscr{I}_\perp(\dot{\gamma})/\mathscr{I}_\perp(0)]_{TCP}\cong 10$ was estimated from Fig. 6, respectively.

The ratio of mean-squared thermal concentration fluctuations, $\langle \Delta\phi^2(0)\rangle_{DOP}/\langle \Delta\phi^2(0)\rangle_{TCP}$, at $T=27\ ^\circ C$ is larger than 1 because PS/DOP is closer to its critical temperature than PS/TCP. Therefore, the ratio of the amplitude of concentration fluctuations $\langle \Delta\phi^2\rangle^{1/2}$ for PS/DOP and PS/TCP at $\dot{\gamma}=1\ s^{-1}$ is larger than about 7, as described in Sec. V A.

[1] H.-L. Wu, D. J. Pine, and P. K. Dixon, Phys. Rev. Lett. **66**, 2408 (1991).
[2] T. Hashimoto and K. Fujioka, J. Phys. Soc. Jpn. **60**, 356 (1991).
[3] T. Hashimoto and T. Kume, J. Phys. Soc. Jpn. **61**, 1839 (1992).
[4] S. Saito, K. Matsuzaka, and T. Hashimoto, Macromolecules **32**, 4879 (1999).
[5] B. A. Wolf, Macromolecules **17**, 615 (1984).
[6] H. Yanase, P. Moldenaers, J. Mewis, V. Abetz, J. van Egmond, and J. J. Fuller, Rheol. Acta **30**, 89 (1991).
[7] F. Boue and P. Lindner, Europhys. Lett. **25**, 421 (1994).
[8] I. Morfin, P. Lindner, and F. Boue, Macromolecules **32**, 7208 (1999).
[9] S. Saito, T. Hashimoto, I. Morfin, P. Lindner, and F. Boue, Macromolecules **35**, 445 (2002).
[10] S. Saito and T. Hashimoto, J. Chem. Phys. **114**, 10531 (2001).

[11] E. Helfand and G. H. Fredrickson, Phys. Rev. Lett. **62**, 2468 (1989).
[12] S. T. Milner, Phys. Rev. E **48**, 3674 (1993).
[13] A. Onuki, Phys. Rev. Lett. **62**, 2472 (1989).
[14] M. Doi and A. Onuki, J. Phys. II **2**, 1631 (1992).
[15] H. Ji and E. Helfand, Macromolecules **28**, 3869 (1995).
[16] S. Saito, M. Takenaka, N. Toyoda, and T. Hashimoto, Macromolecules **34**, 6461 (2001).
[17] A. Kaye, Note No. 134, 1962 (unpublished).
[18] B. Bernstein, E. A. Kearsley, and L. J. Zapas, Trans. Soc. Rheol. **7**, 391 (1963).
[19] R. G. Larson *The Structure and Rheology of Complex Fluids* (Oxford University Press, New York, 1998).
[20] K. Oaski, Rheol. Acta **32**, 429 (1993).
[21] K. Oaski, T. Inoue, T. Uematsu, and Y. Yamashita, J. Polym. Sci., Part B: Polym. Phys. **40**, 1038 (2002).
[22] T. Inoue, Y. Yamashita, and K. Oaski, Macromolecules **35**, 1770 (2002).
[23] M. K. Endoh, S. Saito, and T. Hashimoto, Macromolecules **35**, 7692 (2002).
[24] K. Matsuzaka and T. Hashimoto, Rev. Sci. Instrum. **70**, 2387 (1999).
[25] T. Inoue, Y. Yamashita, H. Watanabe, M. K. Endoh, and T. Hashimoto, Macromolecules **37**, 4317 (2004).
[26] According to the Rouse theory, the storage modulus G' has the power law behavior with ω in the high frequency region, which is described as $G'(\omega)=(1.11cRT/M)(\tau_R\omega)^{1/2}$, where c is the polymer concentration, R is the gas constant, T is the absolute temperature, and M is the molecular weight. Osaki *et al.* focused on this high frequency Rouse region where $G'(\omega)$ is measured as $G'(\omega)=a\omega^{1/2}$ (a is a coefficient) and evaluated the Rouse time τ_R as $\tau_R=\{aM/(1.11cRT)\}^2$.
[27] K. Osaki, T. Inoue, T. Uematsu, and T. Isomura, J. Polym. Sci., Part B: Polym. Phys. **38**, 1917 (2000).
[28] K. Osaki, T. Inoue, T. Uematsu, and Y. Yamashita, J. Polym. Sci., Part B: Polym. Phys. **39**, 1704 (2001).
[29] T. Kume, T. Hattori, and T. Hashimoto, Macromolecules **30**, 427 (1997).
[30] J. Brandrup, E. H. Immergut, and E. A. Grulke, *Polymer Handbook*, 4th ed. (Wiley-Interscience, New York, 1998), p. V/93.
[31] S. Budavari, *The Merck Index*, 13th ed. (Merck, Whitehouse Station, NJ, 2001).
[32] T. Kume and T. Hashimoto, *Flow-Induced Structure in Polymers*, ACS Symposium Series Vol. 597 (ACS, Washington, DC, 1995), p. 35.
[33] From transient behavior of σ and N_1, we observed the second overshoot, which may correspond to the shear-induced structure formation, in the shear rate region between 31.6 and 56.2 s^{-1}: M. K. Endoh, M. Takenaka, T. Inoue, H. Watanabe, and T. Hashimoto (in preparation).
[34] M. Bercea, C. Peite, B. Simionescu, and P. Navard, Macromolecules **26**, 7095 (1993).
[35] J. J. Magda, C. S. Lee, S. J. Muller, and R. G. Larson, Macromolecules **26**, 1696 (1993).
[36] D. W. Mead, R. G. Larson, and M. Doi, Macromolecules **31**, 7895 (1998).
[37] G. Marrucci and N. Grizzuti, Gazz. Chim. Ital. **118**, 179 (1988).
[38] D. S. Person, E. Herbolzheimer, N. Grizzuti, and G. Marrucci, J. Polym. Sci., Part B: Polym. Phys. **29**, 1589 (1991).
[39] T. Kume, T. Hashimoto, T. Takahashi, and G. G. Fuller, Macromolecules **30**, 7232 (1997).
[40] After the cessation of shear at $\dot{\gamma}>\dot{\gamma}_a$, the shear SALS and OM image relax in about 200 s, while σ and N_1 relax in about 100 s.
[41] D. Wirtz, Phys. Rev. E **50**, 1755 (1994).
[42] D. Wirtz, Macromolecules **27**, 5639 (1994).